

Computational Electromagnetic Modelling of Compact Antenna Test Range Quiet Zone Probing

C. G. Parini¹, R. Dubrovka¹, and S. F. Gregson²

¹ School of Electronic Engineering and Computer Science
Queen Mary University of London, London, E1 4FZ, UK
c.g.parini@qmul.ac.uk, r.dubrovka@qmul.ac.uk

² Nearfield Systems Inc.
19730 Magellan Drive, Torrance, CA, 90502, USA
sgregson@nearfield.com

Abstract — This paper extends the authors previous simulation study [1, 2] that predicted the quality of the pseudo plane wave of an offset compact antenna test range (CATR). In this paper, the quiet-zone performance predictions are extended to rigorously incorporate the effects of probing the CATR quiet-zone using various field probes. This investigation leads to recommendations as to the optimal field probe choice and measurement uncertainties. The results of these new simulations are presented and discussed.

Index Terms — Compact antenna test range, field-probe, quiet-zone probing, reaction theorem.

I. INTRODUCTION

The single-offset compact antenna test range (CATR) is a widely deployed measurement technique for the broadband characterization of electrically large antennas at reduced range lengths. The CATR collimates the quasi-spherical wave radiated by a low gain feed into a pseudo transverse electric and magnetic (TEM) plane-wave. The coupling of this locally plane-wave into the aperture of an antenna under test (AUT) creates the classical measured “far-field” pattern. The accuracy of an antenna measured using a CATR is therefore primarily determined by the uniformity of the amplitude and phase of this illuminating pseudo plane-wave.

Traditionally, the quality of the pseudo plane wave has been assessed by “probing” the amplitude and phase across a transverse planar surface with the results being tabulation on, typically, a plane-polar grid consisting of a series of linear scans in the horizontal, vertical and perhaps inter-carinal planes. A number of workers have utilized portable planar near-field antenna test systems to acquire two-dimensional plane-rectilinear data sets that can be used to provide far greater insight into the behavior of the field in the quiet-zone (QZ) and additionally for the purposes of chamber imaging to

provide angular image maps of reflections [3]. However, when mapping the CATR QZ the finitely large aperture of any realized field probe will inevitably affect the mapped fields by way of the convolution process between the pseudo plane wave of the CATR and the aperture illumination function of the scanning near-field probe, *cf.* [4] Potentially, such a discrepancy can lead to confusion when comparing CATR QZ predictions obtained from standard computational electromagnetic (CEM) models and empirical measurements as this “boxcar” field averaging process is not automatically incorporated within the numerical simulation. Several authors have undertaken CATR performance prediction modeling [7, 8, 9] with increasing levels of complexity. This paper extends our recently published comprehensive CATR QZ performance prediction software tool [1, 2] to incorporate the directive properties of several commonly used field probes so that recommendations can be made as to the most appropriate probe to use as well as providing estimates for the upper bound measurement uncertainty.

II. CATR QZ SIMULATION

The field illuminating the CATR offset parabolic reflector is typically derived from the assumed known far-field pattern of the feed antenna. This pattern could be derived CEM simulation, as is the case here, or from empirical range measurements. Figure 1 contains a mechanical drawing of the WR430 choked cylindrical waveguide feed that was used during these simulations with the realised feed shown in Fig. 2. Here, the feed is assumed nominally vertically polarised within its local coordinate system. When computing CATR QZ simulations for a horizontally polarised feed a vector isometric rotation [4] can be used to rotate the probe by 90° about its local z-axis so as to produce equivalent far-field patterns for a horizontally polarised probe.

Figures 3 and 4 respectively illustrate the far-field

amplitude and phase cardinal cuts of the feed antenna when resolved onto a Cartesian polarisation basis. These patterns were obtained from a proprietary three-dimensional full-wave CEM solver that used the finite difference time domain (FDTD) method. Here, the difference in beam-widths is exacerbated by presenting the patterns resolved onto a Cartesian polarisation basis [4].



Fig. 1. Model of WR430 CATR feed.



Fig. 2. Realised WR430 CATR feed.

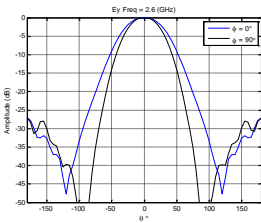


Fig. 3. Amplitude cardinal cuts of feed at 2.6 GHz.

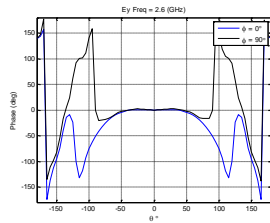


Fig. 4. Phase cardinal cuts of feed at 2.6 GHz.

The location of the phase centre was determined by means of a best fit parabolic function over the $-50^\circ \leq \theta \leq 50^\circ$ angular range [5]. The maximum polar angle of 50° was selected as this is the maximum angle subtended at the feed by the CATR parabolic reflector. For angles larger than this, the feed pattern spills over from the reflector and the feed pattern function for angles larger than this are unimportant. Here, the phase centre of this circular feed was determined as being at $x = y = 0$ m and $z = -0.1377$ m and was found to be extremely stable across the operating bandwidth. The phase patterns were compensated for this parabolic phase function which conceptually corresponds to installing the phase centre of the feed at the focus of the CATR parabolic reflector. The field illuminating the parabolic reflector can then be determined from far-field antenna pattern function by reintroducing the (conventionally suppressed) spherical phase function and the inverse r term. The corresponding magnetic field, as required by the field propagation algorithm, can be computed from the electric field from the TEM far-field condition [4].

As a result of the requirement to minimise feed induced blockage, as described in [1, 2], a single offset reflector CATR design is harnessed. Here, it is assumed that the vertex of the reflector is coincident with the bottom edge of the main reflector. Thus, the feed is

required to be tilted up in elevation so that the boresight direction of the feed is orientated towards the centre of the reflector surface. In this case, the CATR main reflector is formed from an offset parabolic reflector with a focal length of $12' = 3.6576$ m. The reflector was 4.71 m wide by 3.9 m high with serrations of 0.76 m in length. The following figure shows a false-colour plot of the magnitude of the illuminating electric field as radiated by the WR430 feed. Here, the boresight direction of the feed is pointing through the geometric centre of the reflector which corresponds to an elevation tilt angle of approximately 28° . Although this is a non-optimum illumination angle, in actuality a larger elevation angles is used to improve the CATR QZ amplitude taper by compensating for the spherical loss factor, this value was used for the sake of consistency with prior simulations [1, 2]. Within Fig. 5, the white space corresponds to regions where the reflectivity of the reflector is zero. Figure 6 shows an image of the reflector once installed within the test chamber.

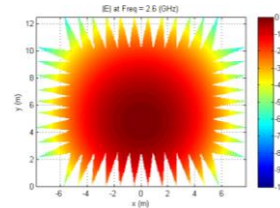


Fig. 5. Magnitude of incident electric field.



Fig. 6. Realised CATR main reflector.

The current element method [1, 2, 6] replaces fields with an equivalent surface current density \underline{J}_s which is used as an equivalent source to the original fields. The surface current density across the surface of the reflector can be obtained from the incident magnetic fields and the surface unit normal using,

$$\underline{J}_s = 2\hat{n} \times \underline{H}_i = 2\hat{n} \times \underline{H}_r. \quad (1)$$

The surface current density approximation for \underline{J}_s (as embodied by the above expression) is known as the physical-optics approximation and allows for the computation of valid fields outside of the deep shadow region. The infinitesimal fields radiated by an electric current element can be obtained from the vector potential and the free-space Green's function [1, 6],

$$d\underline{H}(P) = \frac{da}{4\pi} \underline{J}_s \times \nabla \psi. \quad (2)$$

This is an exact equation. When the field point is more than a few wavelengths from the radiating elemental source, the corresponding elemental electric fields can be obtained conveniently from the elemental magnetic fields using the far-field TEM condition using,

$$d\underline{E} = Z_0 (d\underline{H} \times \hat{u}). \quad (3)$$

Thus, both the electric and magnetic fields can be obtained from the elemental fields by integrating across

the surface of the parabolic reflector. In practice, for the case of a CATR with a QZ located at a distance z that is larger than the focal length of the reflector, the difference between the electric field as computed using the TEM condition and the exact formula is typically on the order of the limit of double precision arithmetic with this error being negligible. Figures 7 and 8 contain respectively false colour plots of the amplitude and phase patterns of the horizontally polarised electric field components of the pseudo-plane wave over the surface of a transverse plane located down-range at $z = 1.8f$, where f is the focal length of the CATR reflector at a frequency of 2.6 GHz. Figures 7, 8, 9 and 10 contain the E_x and E_y polarised amplitude and phase patterns for the horizontally polarised feed case. Although not shown, the equivalent magnetic fields were also computed. When interpreting these plots it is important to recognise that these are the fields one would measure if an infinitesimal electric (*i.e.*, Hertzian) dipole probe were used to sample the QZ fields [4]. This is in agreement with theory and standard CEM modelling tools. In practice, it is not possible to use an infinitesimal current element as a field probe and the following section examines how these patterns can be modified to include the effects of a finitely large, *i.e.*, directive, field probe.

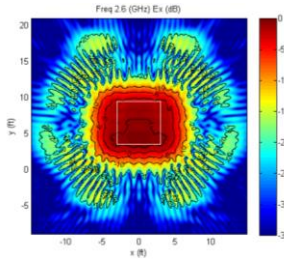


Fig. 7. E_x polarised QZ electric field amplitude.

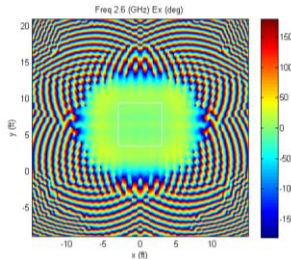


Fig. 8. E_x polarized QZ electric field phase.

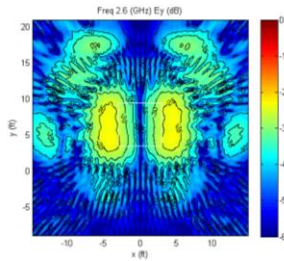


Fig. 9. E_y polarized QZ electric field amplitude.

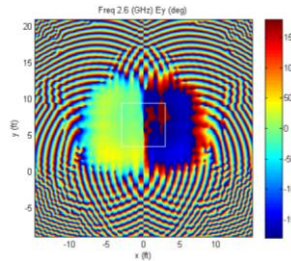


Fig. 10. E_y polarised QZ electric field phase.

III. CATR QZ PROBING SIMULATION

CATR QZ probing is usually accomplished by translating a field probe across a plane that is transverse to the z -axis of the CATR at several positions down-range. An example of a CATR QZ field probe can be seen presented in Fig. 11. Here, the electrically small

field probe can be seen positioned at the limit of travel of the 6' linear translation stage. Generally, pyramidal horns, *e.g.*, *circa* 16 dBi standard gain horns (SGH) [6], are used as CATR QZ probes as they have excellent polarisation purity, are easy to align, have some gain and therefore provide some immunity from reflections from the side and back walls of the anechoic chamber. An alternative choice of field probe is a *circa* 6 dBi gain open ended rectangular waveguide probe (OEWG) [6].



Fig. 11. CATR QZ field being probed using a linear translation stage and a plane-polar acquisition scheme.

The clear difference in the electrical size of aperture of these two antennas and their directive properties and spatial filtering can be expected to result in some differences being observed between the probe measured QZ fields with the effects being quantifiable through an application of the reaction theorem which is a well-known method for analyzing general coupling problems [2, 4]. This theorem states that, provided the electric and magnetic field vectors ($\underline{E}_1, \underline{H}_1$) and ($\underline{E}_2, \underline{H}_2$) are of the same frequency and are monochromatic, then the mutual impedance, Z_{21} , between two radiators, *i.e.*, antennas 1 and 2, in the environment described by ϵ, μ can be expressed in terms of a surface integration [2, 4],

$$Z_{21} = \frac{V_{21}}{I_{11}} = -\frac{1}{I_{11}I_{22}} \int_{S_2} (\underline{E}_2 \times \underline{H}_1 - \underline{E}_1 \times \underline{H}_2) \cdot \hat{n} ds. \quad (4)$$

Here, \hat{n} is taken to denote the outward pointing surface unit normal. The subscript 1 denotes parameters associated with antenna 1 whilst the subscript 2 denotes quantities associated with antenna 2, where the surface of integration encloses antenna 2, but not antenna 1. Here, I_{11} is the terminal current of antenna 1 when it transmits and similarly, I_{22} is the terminal current of antenna 2 when it transmits. Note that this integral does *not* compute transferred power as there are no conjugates present and as such, crucially, phase information is preserved. Here, the fields \underline{E}_1 and \underline{H}_1 are used to denote the CATR QZ whilst fields \underline{E}_2 and \underline{H}_2 denote fields associated with the QZ field probe. From reciprocity, the mutual impedance, $Z_{12} = Z_{21}$, is related to the coupling between the two antennas. Clearly the mutual impedance will also be a function of the displacement between the antennas, their relative orientations, their directivities and their respective polarization properties. Once the

impedance matrix is populated, this can be inverted to obtain the admittance matrix whereupon the required scattering matrix can be computed [4]. The elements $S_{1,2} = S_{2,1}$ of this two port scattering matrix are the complex transmission coefficients for the coupled antenna system which represent a single point in the quiet-zone probing measurement. Although the integration can be performed across any convenient free-space closed surface, in this application integrating across the planar aperture of the OEWG or SGH antenna is perhaps the most computationally efficient strategy. Aperture fields can be obtained from analytical models [4] as in this case, from CEM simulation [4] or from measurement with the choice being determined by the accuracy needed and the available information.

Figure 12 presents a comparison of the CATR QZ amplitude horizontal cut as obtained using an infinitesimal electric dipole (red trace) and an equivalent cut as obtained by using an OEWG probe (blue trace). A measure of the similarity between the respective measurements is provided by the equivalent multipath level (EMPL) [4] (magenta trace). From inspection of Figs. 12 and 13, it is evident that the ideal (dipole) and OEWG measurements are in very good agreement, both in amplitude and phase for the horizontal cuts. This is further confirmed by the EMPL level that is at or below -60 dB right across the pattern peak which corresponds to the useable QZ region.

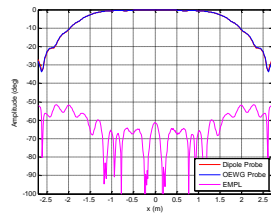


Fig. 12. Horizontal amplitude cut using dipole and OEWG field probe.

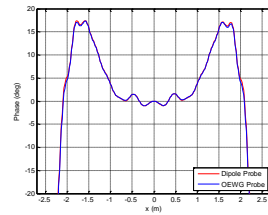


Fig. 13. Horizontal phase cut using dipole and OEWG field probe.

Figures 14 and 15 contain equivalent figures for the case where a SGH has been used as a pyramidal horn probe. Here it is evident from inspection of the amplitude and phase results that the high spatial frequency information within the QZ plots has been attenuated with the larger aperture effectively averaging out the measured response and thereby reducing the observed amplitude and peak-to-peak phase ripple. This is further confirmed by the circa 15 dB increase in the EMPL level between dipole probe and horn probe. Although not shown due to lack of space, equivalent results for the vertical cut exhibited similar phenomena. This probe dependent QZ is a well-known measurement effect but for the first time it has been possible to bound the SGH upper-bound measurement uncertainty and to provide tools necessary for verifying the appropriate choice of field probes.

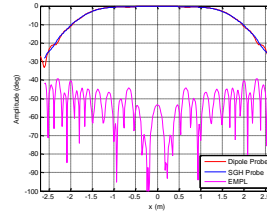


Fig. 14. Horizontal amplitude cut using dipole and SGH probe.

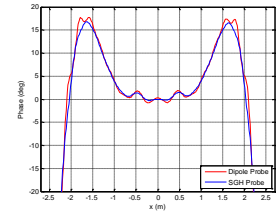


Fig. 15. Horizontal phase cut using dipole and SGH probe.

IV. CONCLUSION

The construction of a complete end-to-end CEM model of a CATR including CATR QZ probing has enabled the validity of standard CATR probing techniques to be objectively and quantitatively examined. Here, it was found that the standard practice of employing a pyramidal horn, e.g., a SGH, as a field probe increases EMPL by *circa* 15 dB by reducing peak-to-peak ripple across the probed QZ. This works also confirmed that an electrically small OEWG probe provides highly accurate measure of the QZ fields with an EMPL < -60 dB and in nearly all the range < -70 dB. As this paper details ongoing research, the planned future work is to include obtaining additional verification of the modeling technique using the alternative plane-wave spectrum scattering matrix representation of antenna-to-antenna coupling.

REFERENCES

- [1] C. G. Parini, R. Dubrovka, and S. F. Gregson, "CATR quiet zone modelling and the prediction of "measured" radiation pattern errors: comparison using a variety of electromagnetic simulation methods," *AMTA*, October 2015.
- [2] C. G. Parini, R. Dubrovka, and S. F. Gregson, "Compact range quiet zone modelling: quantitative assessment using a variety of electromagnetic simulation methods," *LAPC*, November 2015.
- [3] G. E. Hindman and D. Slater, "Anechoic chamber diagnostic imaging," *AMTA Symposium*, 1992.
- [4] S. F. Gregson, C. G. Parini, and J. McCormick, *Principles of Planar Near-Field Antenna Measurements*, IET Press, 2007.
- [5] P. N. Betjes, "An algorithm for automated phase center determination and its implementation," *AMTA Symposium*, 2007.
- [6] C. G. Parini, S. F. Gregson, J. McCormick, and D. Janse van Rensburg, *Theory and Practice of Modern Antenna Range Measurements*, IET Press, 2014.
- [7] M. Philippakis and C. G. Parini, "Compact antenna range performance evaluation using simulated pattern measurements," *IEE Proceedings Microwaves, Antennas and Propagation*, vol. 143, iss. 3, pp. 200-206, 1996, DOI: 10.1049/ip-map:19960398

- [8] C. G. Parini and M. Philippakis, "The use of quiet zone prediction in the design of compact antenna test ranges," *IEE Proc., Microwave Antennas Propagation*, vol. 143, no. 3, pp. 193-199, 1996.
- [9] C. Cappellin, S. Busk Sørensen, M. Paquay, and A. Østergaard, "An accurate and efficient error predictor tool for CATR measurements," 4th EuCAP 2010, Barcelona, 12-16 April 2010.